ARMY RESEARCH LABORATORY

High-Frequency Autofocus Algorithm for Noncooperative ISAR

Geoffrey H. Goldman and Herbert Dropkin

ARL-TR-1890

May 1999

Army Research Laboratory

Adelphi, MD 20783-1197

ARL-TR-1890 **May 1999**

High-Frequency Autofocus Algorithm for Noncooperative ISAR

Geoffrey H. Goldman and Herbert Dropkin

Sensors and Electron Devices Directorate

Approved for public release; distribution unlimited.

Abstract

High-quality automatic target recognition algorithms implemented using a real-beam radar require imagery with resolved target characteristics. This report presents an iterative motion parameter estimation algorithm that improves the quality of high-resolution two-dimensional inverse synthetic aperture radar (ISAR) images. The algorithm uses the derivative of the phase history of isolated point scatterers to estimate the initial conditions for the target motion parameters of a maneuvering vehicle. The algorithm was tested using simulated data. We report on the agreement between the actual and estimated values of range and entropy.

Contents

Figures

Tables

Introduction

Real-beam radars have been used for many years to detect and track moving targets, but their role in automatic target recognition (ATR) has been limited. Typically, the input to ATR algorithms from real-beam radar has been one-dimensional (1-D) high-range resolution profiles. 2-D high-resolution imagery can be obtained from real-beam radar data, but it requires intensive signal processing. Such imagery has the potential to improve ATR algorithm performance in existing systems such as Longbow, Patriot, and other military surveillance radars.

Synthetic aperture radar (SAR) techniques have been extensively studied and many systems have been successfully implemented that generate high-resolution 2-D imagery. The synthetic aperture is typically generated by a side-looking radar within an airplane that is flying in a straight trajectory. The basic scenario describing noncooperative inverse synthetic aperture radar (ISAR) consists of a stationary radar that illuminates a moving target. The radar could be tracking the target or pointed at a fixed location with a target driving through the radar beam. In either case, the processing techniques are very similar. In general, a high ratio of crossrange to downrange motion is desirable.

ISAR images generated with a radar operating at millimeter-wave (MMW) frequencies have advantages and disadvantages over images generated with longer wavelengths. The image resolution in the crossrange direction is proportional to frequency, so higher resolution images can be generated with a higher frequency radar. At higher frequencies, a larger frequency bandwidth is usually available, so higher downrange resolution can also be achieved. The major disadvantages of operating at higher frequencies are increased cost and reduced power. Also, high-frequency radar returns are more sensitive to small changes in the aspect angle of the target. This suggests that images can only be coherently processed over small aspect angles. The algorithm developed in this report uses range-Doppler processing techniques, which also are limited by small angle requirements [1,2].

A major problem associated with imaging a maneuvering vehicle with a real-beam radar is motion compensation. For spotlight mode processing, the phase of the radar signal is compensated to stabilize the center of the scene for SAR and the center of rotation of the target for ISAR. The standard criterion to generate a focused image is that the relative range to the target can be estimated to within $\lambda/16$, where λ is the transmitted wavelength of the radar, which is a difficult criterion to meet at MMW frequencies [3]. SAR algorithms often use the phase gradient autofocus (PGA) technique to improve image quality [4,5]. We used this technique to estimate the derivative of the phase histories of isolated scatterers. Other factors that complicate estimating the motion of the target are the nonuniform target rotation rate, clutter, multipath, and countermeasures. In this report, we describe an algorithm that automatically improves image quality by iteratively estimating the initial condition of four motion parameters.

Simulation

An iterative motion-parameter estimation (IMPE) algorithm was developed and tested on simulated radar data. The major components of the simulation were the target backscatter, target motion, and the radar. The target backscatter was simulated using an N-point, isotropic scatterer model. The simulated radar was modeled after an existing U.S. Army Research Laboratory (ARL) instrumentation radar [6,7]. A simplified target motion model was developed to simulate the 2-D motion of a maneuvering vehicle. Knowledge of the motion model was also used in the IMPE algorithm. Noise was simulated by adding independent and identically distributed (iid) Gaussian random variables to the radar in-phase and quadrature (I&Q) data.

The radar model was configured to match several characteristics of an existing ARL instrumentation radar. The radar is frequency-stepped, pulsed, and coherent. The frequency range of the existing and simulated radar is 33.2 to 34.8 GHz with 256 equally spaced frequency steps. The simulated pulse repetition frequency (PRF) was 70 kHz, which is slower than the maximum PRF of the existing radar, but faster than the maximum speed of the current data acquisition system. We assumed that the antenna pattern was uniform and that a ramp of data could be collected simultaneously. Pulsewidth, polarization, duty cycle, and range ambiguity were not modeled.

Radar backscatter was generated with two different target configurations. The first configuration consisted of 5 scatterers positioned at equal intervals around the circumference of a circle with a radius of 2 m. Each scatterer had a radar cross section (RCS) of 1 m^2. The second configuration consisted of 20 scatterers with random positions and RCS. Their downrange and crossrange positions were randomly determined using a 1-D Gaussian distribution with a mean of 0 m and a standard deviation of 1.5 m. The RCS of the scatterers was randomly determined using a Rayleigh distribution with a mean-square value of 1 m^2.

Simulated radar data were generated by coherently summing the normalized electric fields scattered from each scatterer on the target at discrete times as shown in equations (1) through (3):

$$E\,(t,m) = \sum_{I} \sqrt{\sigma}_i e^{\left(j2k(m)R_i(t)\right)} \ , \tag{1}$$

$$k(m) = \frac{2\pi}{\lambda} = \frac{2\pi\left(f_0 + m\Delta f\right)}{c} \ , \quad \text{and} \tag{2}$$

$$t = nT \ , \tag{3}$$

where E = normalized electric field at t = time for the mth frequency; k = the propagation number, which is a function of m; I = the number of scatterers on the target; σ_i = the RCS of the ith scatterer; R_i = the range of the ith scatterer to the radar; f_0 = the carrier frequency of the radar; m = the number of frequency steps; Δf = the frequency step size; c = the speed of light; n = the radar ramp number; and T = the time to transmit a ramp of data, which is the reciprocal of the pulse PRF. The effect of range on equation (1) was ignored, since the target will be in the far-field.

A simple 2-D motion model was developed to simulate the target trajectory. The model assumes that the target is rigid and that it has constant angular and translational acceleration as illustrated in figure 1. The radar is positioned at the origin of the x, y coordinate system, and the center of rotation of the target is positioned at the origin of the $x1$, $y1$ coordinate system. The distance between these coordinate systems is denoted X_0, which corresponds to the initial range between the radar and the target. The radar coordinate system is fixed, and the target coordinate system is being translated and rotated as a function of time. The initial start time is assumed to be zero, and the target does not move in the Z direction. The velocity and acceleration denoted by V and A in figure 1 describe the translational motion of the target in the $x1$ direction as a function of time. The angular velocity and acceleration denoted by θ and α in figure 1 describe the rotational motion of the $x1$, $y1$ coordinate system.

The model describes the motion of a target using four parameters: velocity, acceleration, angular direction, and turning angle. The turning angle in the model roughly corresponds to the angle of the front wheels of a vehicle relative to its body. The equations of motion ignore effects such as tire side slip. The radius of curvature is estimated from the turning angle and the length between the axles of a vehicle using

$$\rho \approx \frac{L}{2\tan\left(\xi/2\right)} , \tag{4}$$

where ρ = the radius of curvature of the vehicle, ξ = the turning angle of the wheel, and L = the length between the axles of the vehicle. The angular velocity and acceleration of the target can be determined from the radius of curvature and from

$$\omega = \frac{V}{\rho} , \quad \text{and} \tag{5}$$

$$\alpha = \frac{A}{\rho} , \tag{6}$$

where ω = angular velocity, α = angular acceleration, V = velocity, and A = acceleration. The angle and velocity of the target coordinate system as a function of time is described by

$$\theta(t) = \theta + \omega t + \alpha\frac{t^2}{2} , \quad \text{and} \tag{7}$$

$$V(t) = V + At . \tag{8}$$

Figure 1. Radar and target coordinate systems.

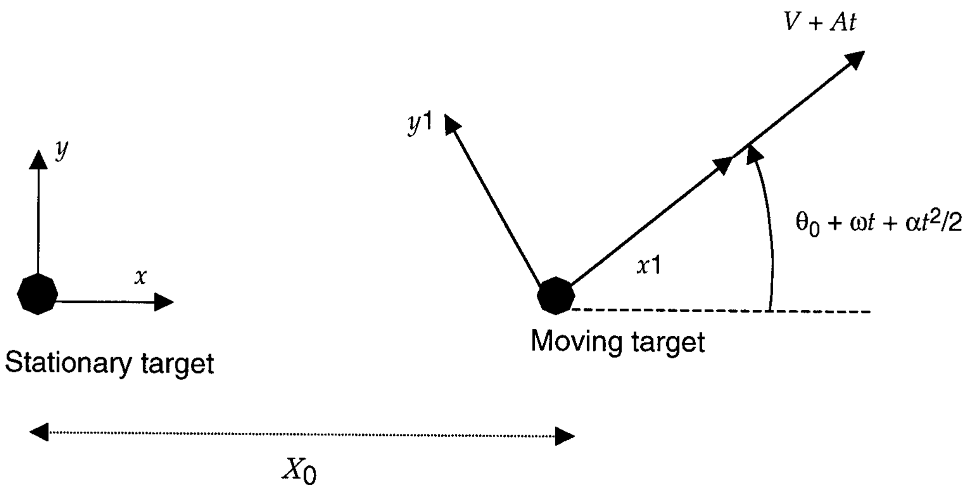

The x and y components of the velocity were calculated using standard trigonometry. The acceleration was calculated by differentiating the velocity with respect to time. The results were then evaluated at $t = 0$, as shown in equations (9) through (12)

$$V_x(0) = V\cos(\theta)\,, \tag{9}$$

$$V_y(0) = V\sin(\theta)\,, \tag{10}$$

$$A_x(0) = \frac{d}{dt}\left(V_x(t)\right) = -V\sin(\theta)\omega + A\cos(\theta)\ \text{, and} \tag{11}$$

$$A_y(0) = \frac{d}{dt}\left(V_y(t)\right) = V\cos(\theta)\omega + A\sin(\theta)\ . \tag{12}$$

The range from the radar to the center of rotation of the target as a function of time can be approximated by applying the Euclidean distance formula to the x and y position of the target:

$$R_0(t) \approx \left(\left(X_0 + V_x t + A_x\frac{t^2}{2}\right)^2 + \left(V_y t + A_y\frac{t^2}{2}\right)^2\right)^{\frac{1}{2}}\ , \tag{13}$$

where X_0 is initial range from the radar to the target. Next, a first-order Taylor series expansion is performed on equation (13). We assume that $X_0 >> \left(V_{t_f} + A\frac{t_f^2}{2}\right)$, where t_f = final imaging time. Applying these approximations to equation (13) and keeping only the coefficients up to t^2, results in

$$R_0(t) \approx X_0 + V\cos(\theta)t + \left(-V\sin(\theta)\omega + A\cos(\theta) + \frac{V^2\sin^2(\theta)}{X_0}\right)\frac{t^2}{2}\ . \tag{14}$$

This equation will be used to estimate the effects of motion-parameter errors on the range.

The target radar model consisted of N isotropic point scatterers that were fixed on the target. The position of the ith scatterer on the target with respect to the radar can be determined by adding the x and y components of the distance between the radar and the center of rotation of the target to the distance between the center of the target to the ith scatterer. This is illustrated by equations (15) and (16):

$$X_i(t) = X_0(t) + x_i(t)\text{, and} \tag{15}$$

$$Y_i(t) = Y_0(t) + y_i(t)\,. \tag{16}$$

The position of the ith scatterer can be described in the polar coordinate system by

$$x_i(t) = r_i\cos\big(\phi_i(t)\big)\ , \tag{17}$$

$$y_i(t) = r_i\sin\big(\phi_i(t)\big)\ ,\ \text{and} \tag{18}$$

$$\phi_i(t) = \phi_i + \omega t + \alpha\frac{t^2}{2}\ , \tag{19}$$

where r_i = the distance from the center of rotation of the target to the ith scatterer, ϕ_i = the initial angle of the ith scatterer in the $x1$, $y1$ coordinate system, ω = angular velocity, and α = angular acceleration. The first and second derivatives with respect to time were calculated for equations (17) and (18), and evaluated at $t = 0$ as shown below:

$$\dot{x}_i(0) = -r_i\sin\big(\phi_i\big)\omega\ , \tag{20}$$

$$\dot{y}_i(0) = -r_i\cos\big(\phi_i\big)\omega\ , \tag{21}$$

$$\ddot{x}_i(0) = -r_i\cos\big(\phi_i\big)\omega^2 - r_i\sin\big(\phi_i\big)\alpha\ \text{, and} \tag{22}$$

$$\ddot{y}_i(0) = -r_i\sin\big(\phi_i\big)\omega^2 + r_i\cos\big(\phi_i\big)\alpha\ . \tag{23}$$

The range to the ith scatterer can be approximated by calculating the Euclidean distance of the components described by equations (15) and (16) using

$$R_i(t) \approx \left(\left(X_0 + V_x t + A_x\frac{t^2}{2} + x_i + \dot{x}_i t + \ddot{x}_i\frac{t^2}{2}\right)^2 + \left(V_y t + A_y\frac{t^2}{2} + y_i + \dot{y}_i t + \ddot{y}_i\frac{t^2}{2}\right)^2\right)^{\frac{1}{2}}\ , \tag{24}$$

where the coefficients are described in equations (9) through (12), (17), (18), and (20) through (23). The difference in range from to the *i*th scatterer to the range of the center of rotation of the target can be computed by subtracting equation (14) from (24) using

$$\Delta R_i(t) = R_i(t) - R_0(t) \,. \tag{25}$$

To produce a polynomial equation as a function of time, a Taylor series expansion was performed on both terms in equation (25). The expansion of $R_0(t)$ was previously calculated in equation (14), and a Taylor series expansion of $R_i(t)$ can be performed if it is assumed that

$X_0 >> \left(V_{t_f} + A \frac{t_f^2}{2} + r_i + \dot{r}_i t_f + \ddot{r}_i \frac{t_f^2}{2} \right)$, where t_f is the final imaging time

and the higher order terms are small. The results are

$$\Delta R_i(t) \approx x_i + \dot{x}_i t + \ddot{x}_i \frac{t^2}{2} + \frac{1}{X_0}\left(y_i V_y + y_i \dot{y}_i\right)t + \frac{1}{X_0}\left(y_i A_y + 2\dot{y}_i V_y + \dot{y}_i^2 + y_i \ddot{y}_i\right)\frac{t^2}{2} \,. \tag{26}$$

If the target motion parameters are incorrectly estimated, then additional terms are required to describe the range to the center of rotation of the target. The actual range to the center of rotation to the target can be decomposed into an estimated range and a range-error term using

$$R_0(t) = \hat{R}_0(t) + \varepsilon_{R_0}(t) \,, \tag{27}$$

where $\hat{R}_0(t)$ = estimate range and $\varepsilon_{R_0}(t)$ = range error. The range error can be estimated multiplying the motion-parameter errors for velocity, acceleration, turning angle, and angular direction by the partial derivatives of $R_0(t)$ with respect to the target motion parameters:

$$\varepsilon_{R_0}(t) = \Delta V \frac{\partial R_0(t)}{\partial V} + \Delta A \frac{\partial R_0(t)}{\partial A} + \Delta\xi \frac{\partial R_0(t)}{\partial \xi} + \Delta\theta \frac{\partial R_0(t)}{\partial \theta} \,. \tag{28}$$

The results of applying equation (28) to the estimate of $R_0(t)$ described in equation (14) are

$$\begin{aligned} \varepsilon R_0(t) = {} & \left(\Delta V \cos(\theta) - \Delta\theta V \sin(\theta)\right)t + \\ & \left(\begin{array}{c} \Delta A \cos(\theta) - \Delta\theta A \sin(\theta) - \Delta V \sin(\theta)\omega - \Delta\theta V \cos(\theta)\omega - \Delta\omega V \sin(\theta) \\ + \Delta V \dfrac{2V \sin^2(\theta)}{X_0} + \Delta\theta \dfrac{2V^2 \sin(\theta)\cos(\theta)}{X_0} \end{array} \right)\frac{t^2}{2} \,. \end{aligned} \tag{29}$$

The estimated change in range for the *i*th scatterer with respect to the center of rotation of the target can now be determined with the effects of the individual motion-parameter errors included in the calculation. The change in range of the *i*th scatterer after nonexact motion compensation is described by

$$\Delta\hat{R}_i(t) = R_i(t) - \hat{R}_0(t) = R_0(t) + \Delta R_i - R_0(t) + \varepsilon_{R_0}(t) = \Delta R_i + \varepsilon_{R_0}(t) \ , \quad (30)$$

where the last two terms are described by equations (26) and (29).

The phase history of a scatterer can be estimated using techniques such as prominient point processing (PPP) and PGA algorithms [8]. The PGA technique estimates the derivative of the phase history of individual scatterers using

$$\dot{\phi}_i(d) = \mathrm{Imag}\left(\frac{\dot{g}_i(d)g_i^*(d)}{\left|g_i(d)\right|^2}\right) \ , \quad (31)$$

where $g_i\,(d)$ = the crossrange slice at the *d*th bin of the complex image calculated using a 2-D discrete Fourier transform (DFT), dot = derivative, star = complex conjugate, and Imag = imaginary [4]. Equation (30) can be transformed to correspond with equation (31) by multiplying the two-way range by the propagation number and taking the derivative with respect to time as shown below:

$$\dot{\Psi}_i(t) = 2k\Delta\dot{\hat{R}}_i(t) \ . \quad (32)$$

If the scatterer location and the motion-parameter errors are known, then the phase derivative calculation described in equation (31) should be approximately equal to the theoretical result described in equation (32). The scatterer locations can be estimated if motion-parameter errors are known. The next section will describe the algorithm in more detail.

IMPE Algorithm

The IMPE algorithm presented in this report iteratively estimates the initial conditions of four motion parameters. Figure 2 shows a block diagram of the algorithm. The first half of the algorithm, shown on the left side of the figure, describes how information on the phase history of individual point scatterers was estimated. The second half of the algorithm, shown on the right side of the figure, describes how the initial conditions of the motion parameters were estimated. As the estimates of the target motion parameters were improved, the motion compensation correction and the image quality were also improved.

The derivatives of the phase history of individual point scatterers were estimated using equation (31). This equation assumes that there are isolated point scatterers on the target and that they are still recognizable in the ISAR image after nonexact motion compensation. First, the radar data were motion-compensated to stabilize the center of rotation of the target using the best available estimate of the target motion. Next, an image was formed using a 2-D DFT. If this is a "good" image, or if a stopping condition has been met, the algorithm will end. (Currently, the algorithm stops after 60 iterations.) Otherwise, the locations of the target scattering centers were determined by convolving a 2-D Gaussian template with the ISAR image, applying a weighting function, then selecting the elements with the largest magnitude. A fixed-length, uniformly weighted window function was used to extract crossrange data in the ISAR image. The phase derivative was calculated for each scatterer and was fit to a second-order polynomial.

Once the phase derivatives of the scatterers were found, the motion-parameter estimation portion of the algorithm shown on the right side of figure 2 was started. Third polynomials were fit to the results obtained using equation (31), and the zero- and first-order polynomial coefficients were equated to coefficients calculated using equation (32). The zero-order coefficients were used to calculate the crossrange position of the scatterers, and the agreement between the simulated and calculated first-order coefficient was used to evaluate the motion parameters. First, four motion parameters were selected from a 4-D hypercube that was discretely sampled at equal intervals. Next, the crossrange positions of the scatterers in the ISAR image were calculated based on the zero-order polynomial coefficients calculated from the phase derivative of each point scatterer and on the selected motion parameters. The downrange position of the scatterers on the target were calculated by assuming that the average downrange position of the scatterers in the image were located at the center of the target. The agreement between the simulated and calculated first-order coefficients were determined using

$$X_n = \left(\sum_I w_i \left| c_{in} - s_i \right| \right) \left(\left| \left\langle \sum_I y_{in} \right\rangle \right| + \varepsilon \right) , \qquad (33)$$

Figure 2. Block diagram of the IMPE algorithm.

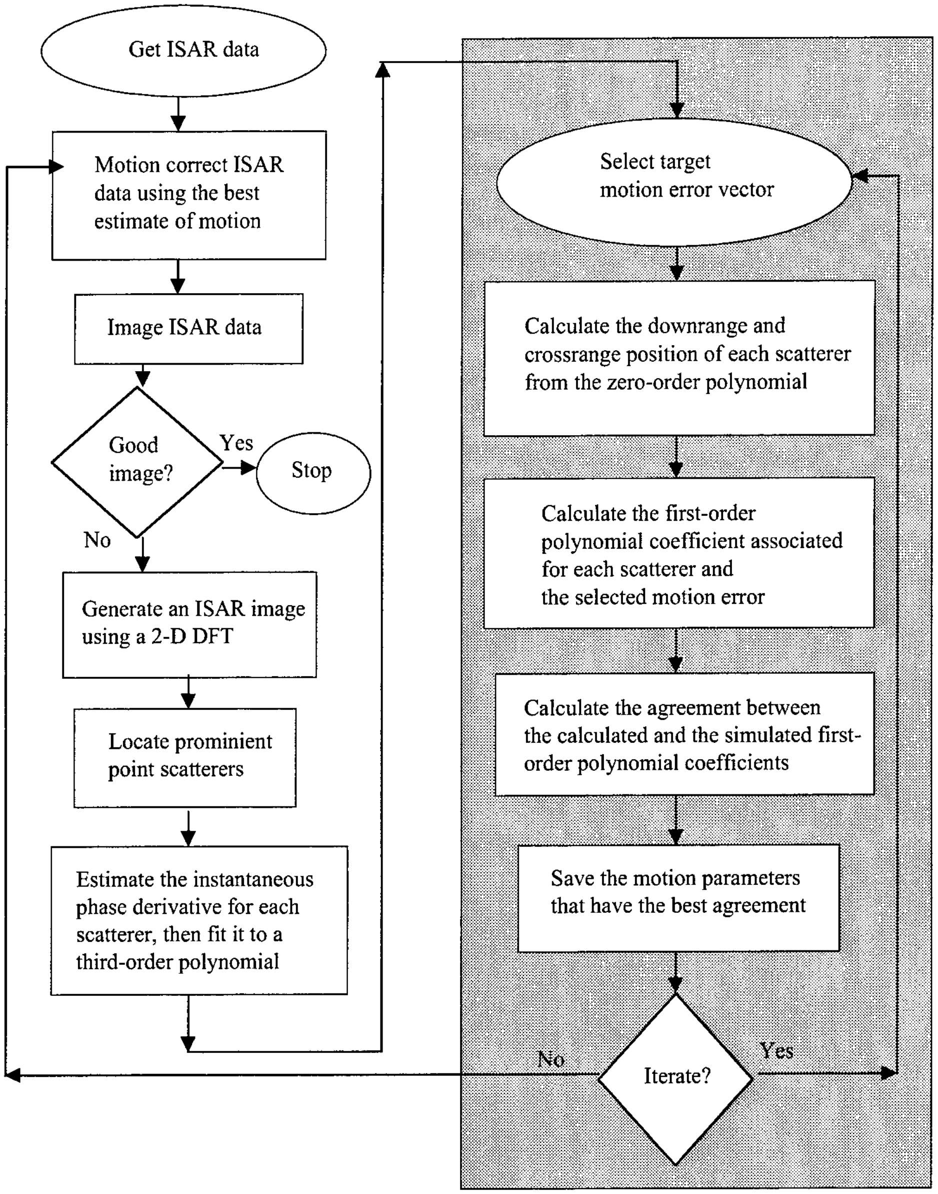

where X_n = the agreement for the *n*th set of motion parameters, w_i = the magnitude from the scatterer selection routine for the *i*th scattering center, c_{in} = the calculated first-order coefficient of the phase derivative for the *i*th scatterer and the *n*th set of motion parameters, s_i = the simulated first-order coefficient of the phase derivative, I = the set of scatterers with the smallest absolute difference between c_{in} and s_i, y_{in} = the crossrange position, and ε = a small positive constant (0.5 m). In the first factor in equation (33), the absolute value of the agreement between the first-order coefficients is calculated. In the second factor, the crossrange position of the scatterers is averaged and added to an offset. This forces the average crossrange position of the scatterers to be near the origin. This is justified if the average scatterer position identified on the target is close to the center of rotation of the target. The motion-parameter vectors with the smallest value of X were saved. For runs using the target configuration with 5 fixed scatterers, the 5 most prominient scatterers were evaluated and the motion-parameter vectors with the three smallest values of X were averaged together to form a new estimate. For runs using the target configuration with 20 random scatterers, the 8 most prominent scatterers were evaluated and the 7 scatterers with the best agreement were used to determined the smallest value of X. The 7 motion-parameters vectors with the smallest values of X were then normalized by subtracting the mean and dividing by the standard deviation. The 6 motion-parameter vectors with the smallest Euclidian distance were averaged to form a new motion-parameter estimate. The updated estimate of the motion parameters are calculated using

$$\hat{p}(n+1) = \hat{p}(n) + u\left(p(n) - \hat{p}(n)\right) , \tag{34}$$

where $\hat{p}(n+1)$ = the new estimated motion-parameter vector, $\hat{p}(n)$ = the previous estimated motion-parameter vector, $p(n)$ = the motion-parameter vector calculated for the nth iteration of the algorithm, and u = the step size parameter equal to 0.1.

The search pattern used by the IMPE algorithm to locate the best motion-parameter vectors was a brute-force method that requires N^4 iterations. Motion parameters were selected from a 4-D hypercube that was discretely sampled at equal intervals. The center of the hypercube was set to the current estimate of the motion parameters, and it extended ±1.5 times the error estimate in the motion parameters. The initial error estimate was equal to the actual error estimate. For successive iterations, the search space for each parameter was linearly reduced. For the last iteration, the range of the search space was ±0.3 times the initial error. This part of the algorithm was implemented with four loops. This is an inefficient searching algorithm, but it reduced the problem of finding local minimums rather than the global minimum. The number of motion-parameter error vectors searched varied from approximately 29,000 to 200,000. More searching was required when there was a less accurate estimate of the motion parameters. Implementation of the IMPE algorithm would require a more intelligent search procedure.

The computational complexity of the entire algorithm was evaluated using the number of arithmetic operations as a criterion. The computational complexity is approximately equal to $L(MN^4O + FR\log(F) + RF\log(R))$, where L = the number of iterations, M = the number of scatterers, N = the number of possible values for each motion parameter, O = the number of operations required to calculate X_n (80 to 100), F = the number of frequencies, and R = the number of ramps. This results in a total of between 5×10^{10} to 8×10^{10} calculations per run. The algorithm took between 3 to 5 hr per run using code written in Matlab, version 5.2.1, on a Pentium II computer running at 333 MHz.

A standard set of motion-parameter values and errors was selected for testing the algorithm. Realistic values were selected for the motion parameters that did not violate any of the assumptions required by the algorithm. The motion errors were selected using the following procedure. First, the maximum error that the IMPE algorithm could correctly compensate for was determined separately for each motion parameter. Then the maximum error for each parameter was reduced by 40 percent and combined to form a motion-parameter error vector. The initial estimate of the range and motion parameters was determined from the sum of the actual values plus the initial errors shown in table 1.

The initial range from the radar to the target was 1 km. The downrange error was equal to the mean downrange position of the scatterers in the ISAR image, since the center of rotation of the target was at the origin. The distance between the axles in the target required by equation (4) was set to 3.5 m and the exact value was used in the algorithm. The results of applying equations (4) through (6) to the parameters selected in table 1 is a radius of curvature of approximately 200 m, angular velocity of 0.05 rad/s, and angular acceleration of 0.005 rad/s^2. The total collection time is equal to the number of frequencies transmitted, multiplied by the number of ramps collected, divided by the PRF of the simulated radar. This results in a simulated collection time or final time t_f, of approximately 0.94 s. The rotation angle, calculated using equation (7), is approximately 0.05 rad, which is much less than 1 rad. The total distance traveled by the target is approximately 10 m, which is much less than the range of 1 km. These calculations indicate that the approximations made in developing the IMPE algorithm are valid. The downrange and crossrange resolution of an ISAR image generated using the radar model and the above target motion values are both approximately 0.1 m.

Table 1. Target motion parameters and initial errors.

Motion parameters	Parameter values	Initial errors
Velocity (V)	10 m/s	0.15 m/s
Acceleration (A)	1 m/s^2	0.3 m/s^2
Angle of wheel	1°	0.41°
Angular direction	60°	–0.26°

Results

The results are presented in two parts: a qualitative section where some intuition can be developed and a quantitative section where two metrics are evaluated. In the qualitative section, ISAR images and the motion parameters are shown in detail for a single run. The images were generated using a 2-D DFT. In the quantitative section, the metrics normalized range error and entropy are evaluated. These metrics were selected because they are relatively simple to calculate, have physical significance, and are related to image quality. When the simulated data were motion-compensated with the exact motion parameter values, the value of both metrics was zero and the image quality was high. The normalized range error and normalized entropy statistics were evaluated for various levels of noise. The range error was calculated by subtracting the estimated range from the exact range at each radar sample time, then the standard deviation was calculated as a function of time, or equivalently, ramp number. The normalized range error was calculated by dividing the range error by the average radar wavelength. The entropy was calculated using

$$H_k = -\Sigma_X \Sigma_Y \, g(x,y) \log(g(x,y)) \, , \tag{35}$$

where H_k = entropy at the kth iteration of the algorithm, $g(x,y)$ = the image of the motion-compensated radar data, and x and y are indices. The entropy was normalized using

$$H_k' = \frac{H_k - H_{\min}}{H_0 - H_{\min}} \, , \tag{36}$$

where H_k' = the normalized entropy, H_k = the entropy at the kth iteration of the algorithm, H_{min} = the entropy (minimum) with exact motion compensation, and H_0 = entropy calculated with the initial motion compensation. The range error and entropy were calculated after each iteration of the algorithm. Perfect motion compensation resulted in zero range error and zero normalized entropy.

Detailed results of the IMPE algorithm are presented for a target RCS model consisting of 20 random scatterers with independent Gaussian noise with a mean of 0 m and variance of 5 m^2. Figure 3 shows range-Doppler images of the target at various stages in the algorithm. Figure 3(a) shows the initial ISAR image with motion compensation that included the errors shown in table 1. Figure 3(i) shows the exact motion compensation. The remaining ISAR images had motion compensation performed using estimates from the IMPE algorithm at various iteration points. These results qualitatively show the improvement in image quality.

Figure 3. Range-Doppler images of 20 random scatterers with Gaussian noise: (a) Initial ISAR image, (b) after 6 iterations, and (c) after 11 iterations.

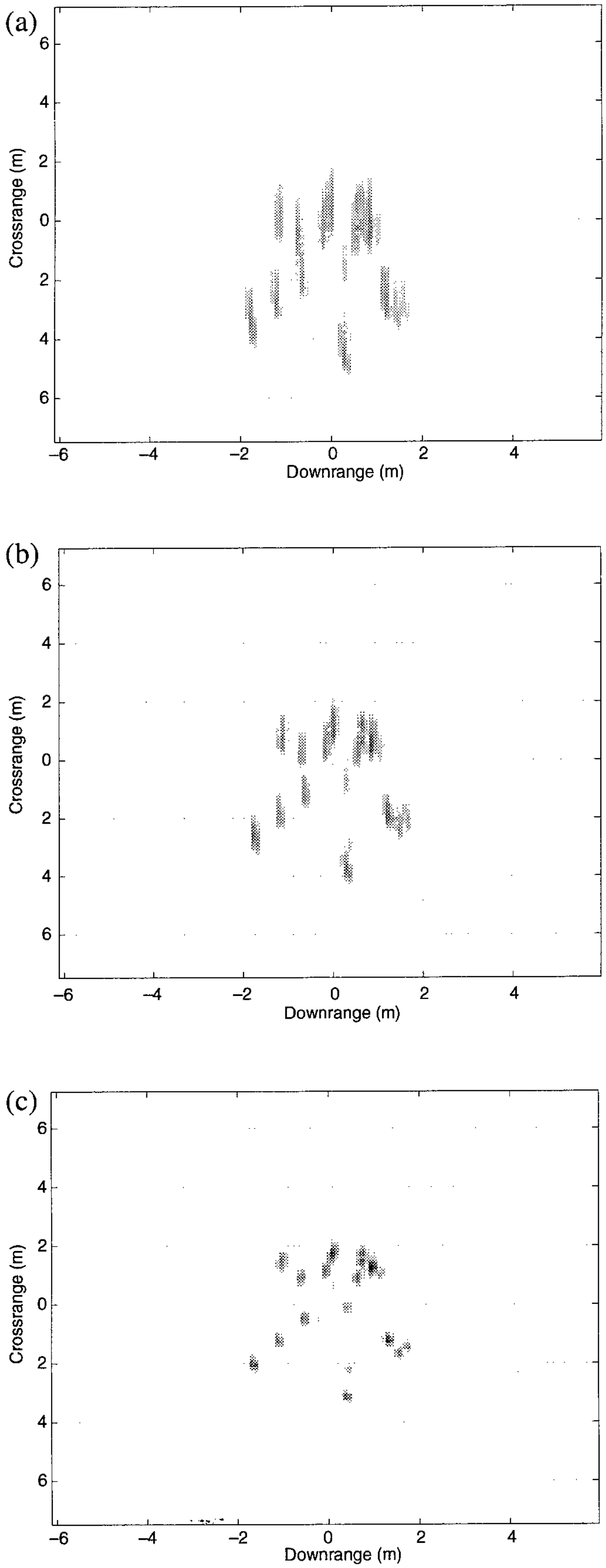

Figure 3 (cont'd). Range-Doppler images of 20 random scatterers with Gaussian noise: (d) after 16 iterations, (e) after 21 iterations, and (f) after 26 iterations.

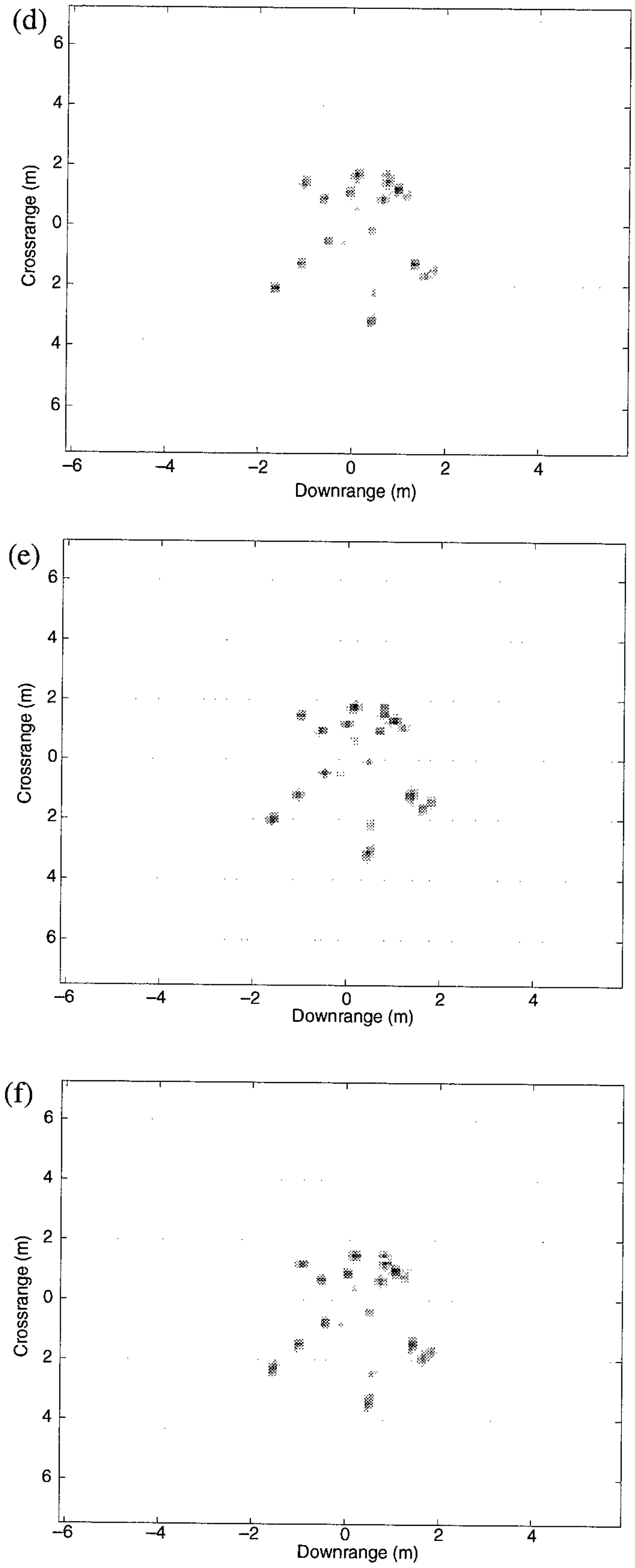

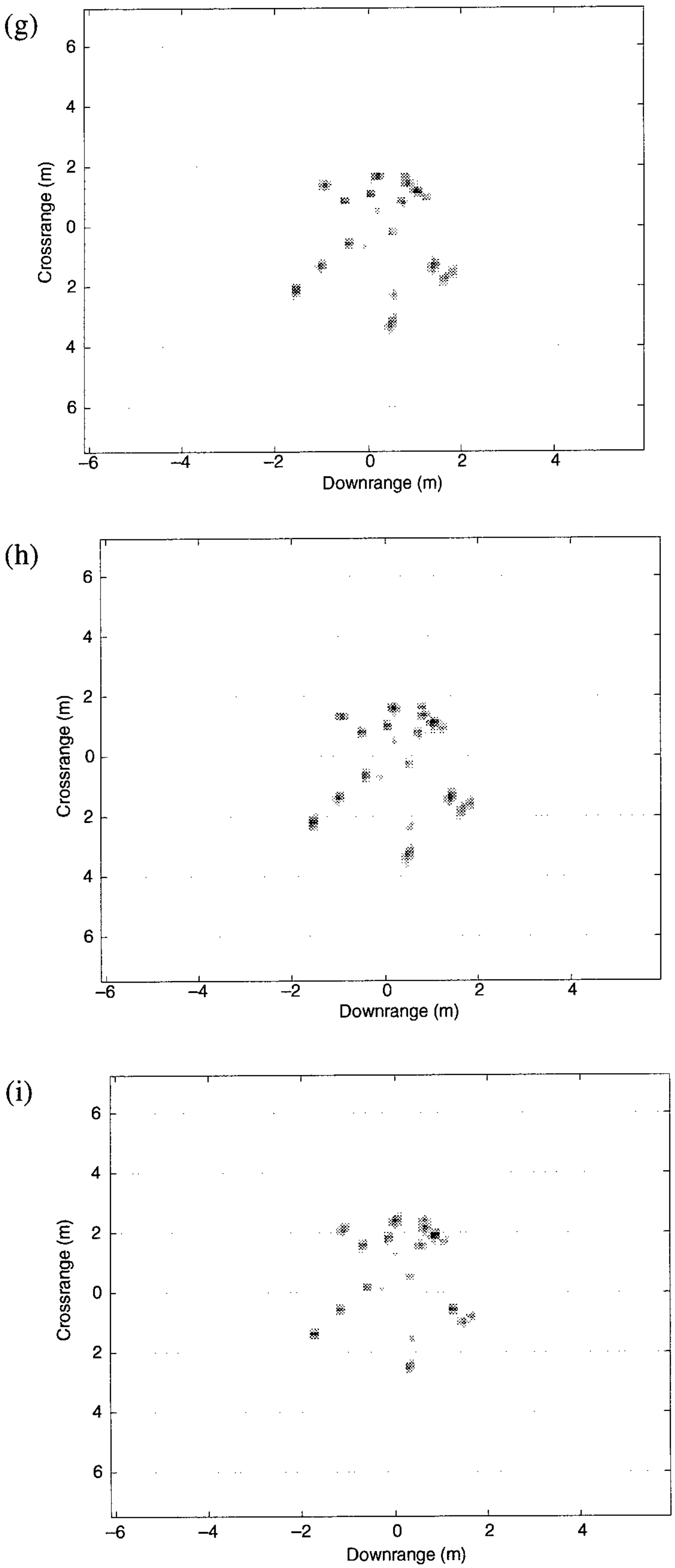

Figure 3 (cont'd). Range-Doppler images of 20 random scatterers with Gaussian noise: (g) after 31 iterations, (h) after 61 iterations, and (i) with exact correction.

It is also informative to examine the estimates of the motion parameters as a function of iteration number. Sometimes, the motion parameters converged to their correct values, but most of the time they did not. Certain combinations of values produced very good range estimates, even though they did not correspond to the actual motion parameters.

For example, a high estimate in velocity could be partially offset by a low estimate in acceleration in the range calculation. Figure 4 shows the normalized error for the four motion parameters. The initial errors shown in table 1 were normalized to a value of 1. Figures 5 and 6 show the normalized range error and the entropy versus algorithm iteration number. These graphs qualitatively indicate that range error and entropy are a better measure of image quality than error in the motion parameters. The motion-parameter errors were often large and had a large variance over several trials.

The algorithm performance was quantitatively analyzed using the normalized range error and entropy, as shown in tables 2 and 3. Ten trials were run for each target configuration and noise level. A visual analysis was performed to eliminate trials where the minimum range error was larger than the other trials. The number of trials eliminated is encapsulated by parentheses in columns two and three of tables 2 and 3. The mean and standard deviation were calculated for the remaining runs. For the fixed target configuration with no noise added, the actual values were reported rather than the statistics.

Figure 4. Normalized motion-parameter errors for a single trial run.

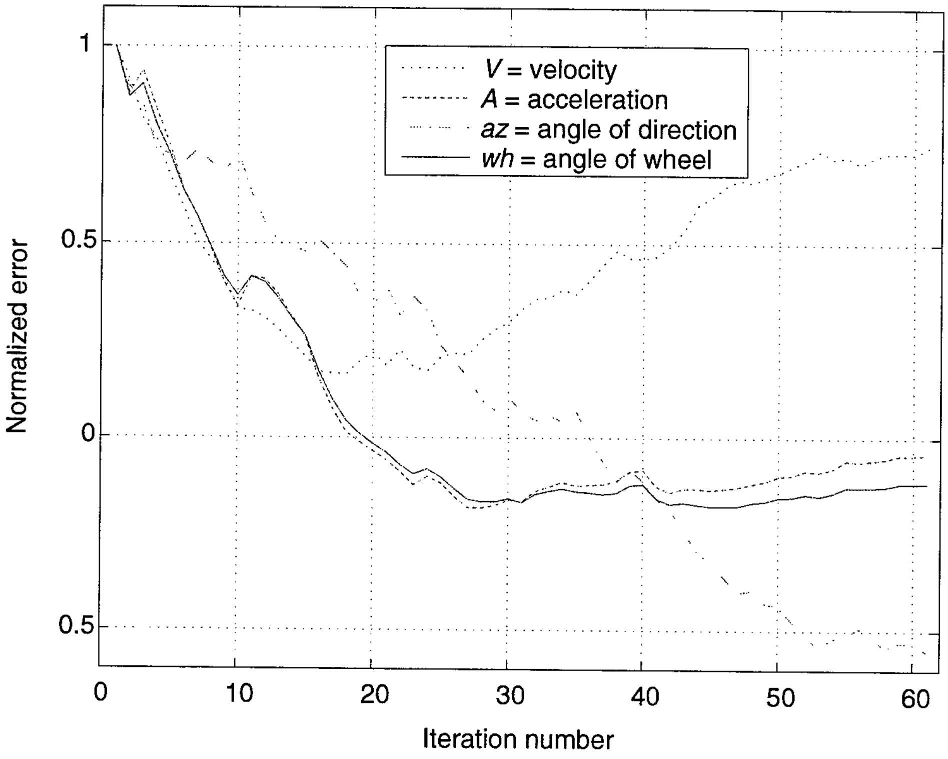

Figure 5. Normalized range error for a single run.

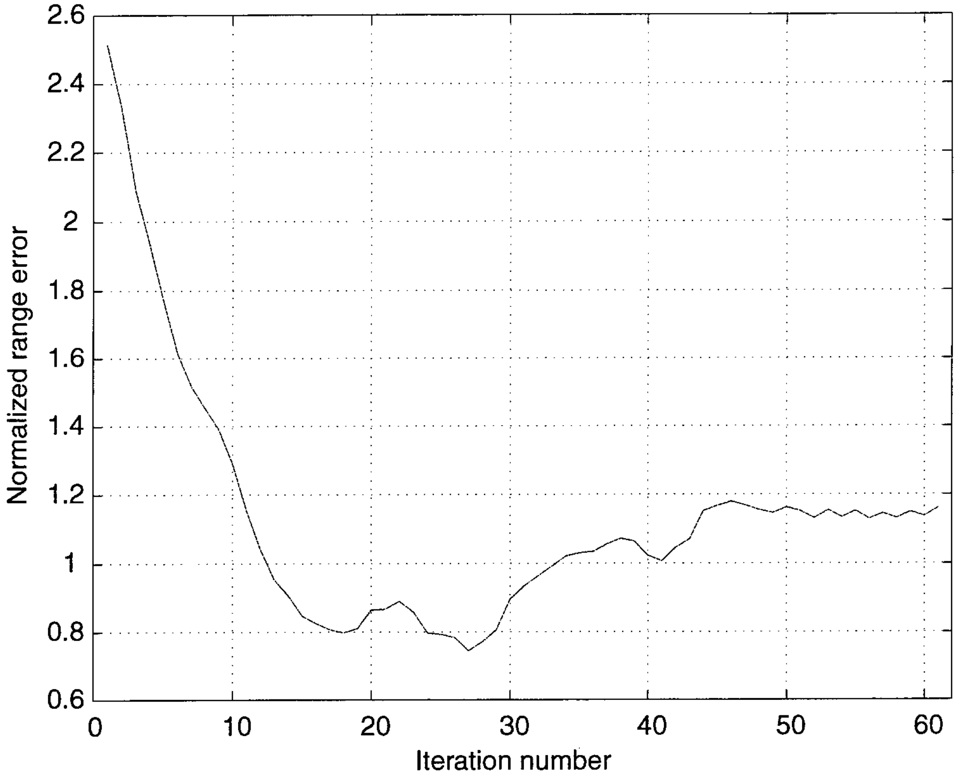

Figure 6. Normalized entropy for a single run.

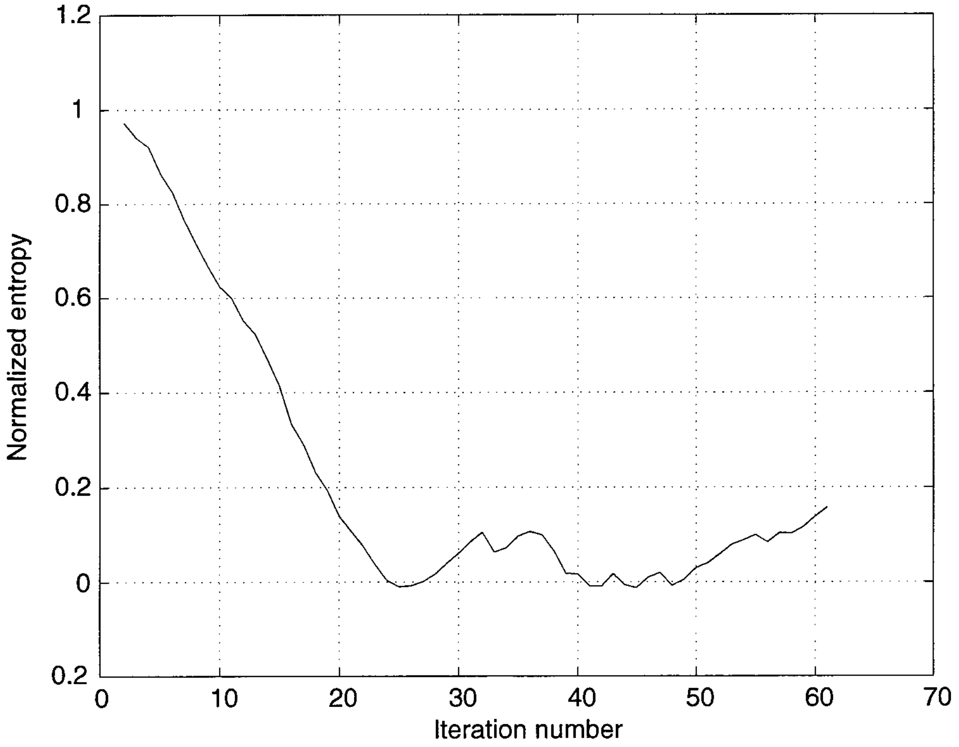

Table 2. Minimum range error normalized by wavelength.

Noise variance (m^2)	Mean ± standard deviation (trials eliminated)	
	5 scatterers	20 random scatterers
0	0.008 (0)	0.18 ± 0.10 (0)
5	0.048 ± 0.027 (1)	0.21 ± 0.10 (1)
20	0.056 ± 0.032 (2)	0.26 ± 0.16 (1)
40	0.087 ± 0.066 (2)	0.25 ± 0.11 (1)
80	0.133 ± 0.107 (2)	0.27 ± 0.11 (1)
160	0.256 ± 0.138 (0)	0.24 ± 0.12 (1)
320	0.249 ± 0.122 (0)	0.27 ± 0.10 (1)
640	0.232 ± 0.129 (0)	0.21 ± 0.11 (1)
1280	0.363 ± 0.212 (0)	0.23 ± 0.12 (1)

Table 3. Minimum normalized entropy.

Noise variance (m^2)	Mean ± standard deviation (trials eliminated)	
	5 scatterers	20 random scatterers
0	0.0027 (0)	0.017 ± 0.05 (0)
5	0.027 ± 0.050 (1)	0.086 ± 0.12 (1)
20	0.051 ± 0.076 (2)	0.31 ± 0.38 (1)
40	0.085 ± 0.12 (2)	0.32 ± 0.40 (1)
80	0.23 ± 0.26 (2)	0.38 ± 0.41 (1)
160	0.52 ± 0.38 (0)	0.34 ± 0.34 (1)
320	0.57 ± 0.38 (0)	0.46 ± 0.41 (1)
640	0.38 ± 0.40 (0)	0.50 ± 0.36 (1)
1280	0.51 ± 0.49 (0)	0.14 ± 0.34 (1)

The results are reported for different noise levels, but they can also be expressed as signal-to-noise (SNR) ratios. The expected values of the RCS of the two target configurations are 5 and 20 m^2. The expected values of the RCS of the noise are 0, 5, 20, 40, 80, 160, 320, and 640 m^2. This results in SNRs of infinite, 0, –6, –9, –12, –15, –18, and –21 dB for the 5 fixed scatterer configuration and infinite, 6, 0, –3, –6, –9, –12, and –15 dB for the 20 random scatterer configuration. Coherent processing gains obtained using 256 frequencies and 256 ramps could potentially improve the SNR by 48 dB. In the simulation, full coherent gains were not achieved. For example, randomly placed scattering centers could interfere with each other, which represented a noise to the algorithm. The initial range error was approximately 2.5 wavelengths. The initial entropy varied depending on the scatterer configuration and on the variance of the noise.

These results indicate that in approximately 80 percent of the runs with 5 fixed scatterers and approximately 90 percent of the runs with 20 random scatterers, the algorithm was able to significantly improve range error and entropy statistics. As the noise levels increased, the number of outliers first increased, then began to decrease. This odd behavior was a result of the threshold for outliers changing, rather than the performance of the algorithm improving.

The results in tables 2 and 3 indicate that the IMPE algorithm significantly improved the evaluation metrics. Higher SNRs produced better metric statistics and image quality. The algorithm also was able to improve estimates of the motion parameters, but often improvements in the metrics did not correspond with improvements in estimates of the motion parameters. This is not a surprising result since four motion parameters were being estimated with a sensor that estimated range. There are many combinations of these motion parameters that could result in very similar estimates of the range.

The range error was usually larger than $\lambda/16$, the standard criterion to generate a focused image. The results in table 2 are reported in range error divided by wavelength, so the normalized range error should be less than 1/16 or 0.0625 for a focused image using the standard criterion. This was only satisfied for the 5 scatterer target configuration with small noise levels. However, there were significant visual improvements in image quality even when this criterion was not satisfied.

In general, the metrics for the 5 fixed scatterer configuration were better than those for the 20 random scatterer configuration. But the 5 fixed scatterer configuration also had more trials eliminated. These results are due to tradeoffs between having isolated scatterers and more scatterers. More scatterers produce increased stability in the algorithm and isolated scatterers produce better metrics and image quality.

Minimum range error and entropy statistics were examined to determine if entropy could be used as a stopping condition for the IMPE algorithm. Table 4 shows the mean and standard deviation for the range error at the minimum entropy, and table 5 shows the mean and standard deviation of the difference between the iteration number corresponding to the minimum range error and the iteration number corresponding to minimum entropy.

These results indicate that minimum normalized entropy and minimum range error are not highly correlated. More sophisticated metrics are required to determine when the algorithm should stop iterating.

Table 4. Range error at minimum entropy.

Noise variance (m^2)	Mean ± standard deviation (trials eliminated)	
	5 scatterers	20 random scatterers
0	0.010	0.81 ± 0.57
5	0.12 ± 0.13	0.86 ± 0.57
20	0.16 ± 0.22	0.80 ± 0.52
40	0.18 ± 0.21	0.66 ± 0.33
80	0.24 ± 0.22	0.98 ± 0.43
160	0.73 ± 0.78	0.98 ± 0.52
320	0.77 ± 0.80	1.09 ± 0.54
640	0.72 ± 0.65	0.95 ± 0.60
1280	1.8 ± 1.6	1.06 ± 0.76

Table 5. Difference in iteration index number of minimum range error and minimum entropy.

Noise variance (m^2)	Mean ± standard deviation (trials eliminated)	
	5 scatterers	20 random scatterers
0	1	–21 ± 16
5	5.9 ± 12	–18 ± 19
20	5.9 ± 20	–21 ± 29
40	0.5 ± 19	–19 ± 22
80	–7.5 ± 23	–14 ± 30
160	–10 ± 25	–17 ± 25
320	-5.0 ± 27	–18 ± 26
640	–11 ± 18	–23 ± 17
1280	1.3 ± 22	–10 ± 32

Conclusions

An iterative motion-parameter estimation algorithm was developed for noncooperative ISAR at MMW frequencies. The algorithm was tested using simulated radar data with various levels of noise. The major components of the simulation were the target backscatter model, the radar model, and the target motion model. Two target RCS configurations were tested: 5 point scatterers located at fixed locations and 20 scatterers located at random locations. The significant parameters of the radar model corresponded to an existing ARL instrumentation radar. A simple 2-D target motion model was developed and reasonable motion-parameter values and errors were selected. Normalized range error and the entropy metrics were used to evaluate the algorithm.

In approximately 80 percent of the runs with 5 fixed scatterers and approximately 90 percent of the runs with 20 random scatterers, the algorithm was able to significantly improve the metrics and the visual image quality. The image focus criterion that required range error of less than $\lambda/16$ was only satisfied for the 5 scatterer target configuration with small noise levels. However, there were significant visual improvements in image quality when this criterion was not satisfied. The algorithm was able to improve estimates of the motion parameters, but the updated values usually did not converge to their actual values. Visual analysis indicated that improvements in image quality often did not correspond with improvements in estimates of the motion parameters. In general, the 5 scatterer target configuration had better image quality than the 20 random scatterer configuration, but it also had more trials eliminated. Minimum entropy was tested as a stopping condition for the algorithm. The results indicated that minimum entropy was not highly correlated with the minimum range error. The metrics selected did not always correspond with visual analysis. Thus, more sophisticated metrics based on specific target recognition algorithm requirements are needed.

Overall, the results were positive enough to warrant further investigation. The algorithm should be tested on real data in a benign environment. If the algorithm performs well, the next step would be to develop a more realistic simulation and to reduce the computation time. More sophisticated target backscatter, motion, and noise and clutter models as well as multipath effects are required. Additional sensors such as a monopulse radar and/or infrared sensors should also be included in the simulation. Also, a more efficient search pattern should be developed for locating motion-parameter corrections.

Acknowledgments

We would like to acknowledge the contributions of Ed Burke whose support allowed this work to be performed. We would like to thank Barry Scheiner for his insights and access to his collection of technical references. We also would like to thank Tom Pizzillo, Roberto Innocenti, Canh Ly, Ragu Damarla, and Jerry Silvious for numerous discussions and ideas. In addition, we also would like to acknowledge the behind-the-scenes contributions of Russ Harris who solved numerous quirky computer problems.

References

1. J. L. Walker, "Range Doppler Imaging of Rotating Objects," *IEEE Aero. & Elect.* **AES-16**, 1 (1980).
2. D. A. Ausherman, A. Kozma, J. L. Walker, H. M. Jones, and E. C. Poggio, "Developments in Radar Imaging," *IEEE Aero. & Elect.* **AES-20**, 4 (July 1984).
3. C. V. Jakowatz, D. E. Wahl, P. H. Eichel, D. C. Ghiglia, and P. A. Thompson, *Spotlight Mode Synthetic Aperture Radar: A Signal Processing Approach*, Kluwer Acedemic Publishers (1996).
4. P. H. Eichel and C. V. Jakowatz, "Phase-Gradient Algorithm as an Optimal Estimator of the Phase Derivative," *Opt. Lett.* **14**, 20 (October 1989), 1101–1103.
5. D. C. Ghiglia and G. A. Mastin, "Two-Dimensional Phase Correction of Synthetic-Aperture-Radar Imagery," *Opt. Lett.* **14**, 20 (October 1989), 1104–1106.
6. S. R. Stratton, H. B. Wallace, R. L. Bender, and A.E.M. Broden, *A Comparison of Radar Cross-Section Measurements of 11 T72M1 Tanks at 35 GHz*, U.S. Army Research Laboratory, ARL-TR-1421 (July 1997).
7. R. L. Bender, *Use of a Remotely Controlled Dihedral for Calibrating a Polarimetric Radar*, U.S. Army Research Laboratory, ARL-MR-318 (June 1996).
8. W. G. Carrara, R. S. Goodman, and R. M. Majewski, *Spotlight Synthetic Aperture Radar*, Artech House (1995), 268–280.

Distribution

Admnstr
Defns Techl Info Ctr
Attn DTIC-OCP
8725 John J Kingman Rd Ste 0944
FT Belvoir VA 22060-6218

Ofc of the Dir Rsrch and Engrg
Attn R Menz
Pentagon Rm 3E1089
Washington DC 20301-3080

Ofc of the Secy of Defns
Attn ODDRE (R&AT) S Gontarek
The Pentagon
Washington

OSD
Attn OUSD(A&T)/ODDR&E(R) R J Trew
Washington DC 20301-7100

AMCOM MRDEC
Attn AMSMI-RD W C McCorkle
Redstone Arsenal AL 35898-5240

CECOM
Attn PM GPS COL S Young
FT Monmouth NJ 07703

Dir for MANPRINT
Ofc of the Deputy Chief of Staff for Prsnnl
Attn J Hiller
The Pentagon Rm 2C733
Washington DC 20301-0300

US Army Armament Rsrch Dev & Engrg Ctr
Attn AMSTA-AR-TD M Fisette
Bldg 1
Picatinny Arsenal NJ 07806-5000

US Army Edgewood RDEC
Attn SCBRD-TD G Resnick
Aberdeen Proving Ground MD 21010-5423

US Army Info Sys Engrg Cmnd
Attn ASQB-OTD F Jenia
FT Huachuca AZ 85613-5300

US Army Natick RDEC Acting Techl Dir
Attn SSCNC-T P Brandler
Natick MA 01760-5002

Director
US Army Rsrch Ofc
4300 S Miami Blvd
Research Triangle Park NC 27709

US Army Simulation, Train, & Instrmntn Cmnd
Attn J Stahl
12350 Research Parkway
Orlando FL 32826-3726

US Army Tank-Automtv Cmnd Rsrch, Dev, & Engrg Ctr
Attn AMSTA-TA J Chapin
Warren MI 48397-5000

US Army Train & Doctrine Cmnd
Battle Lab Integration & Techl Dirctrt
Attn ATCD-B J A Klevecz
FT Monroe VA 23651-5850

US Military Academy
Mathematical Sci Ctr of Excellence
Attn MDN-A MAJ M D Phillips
Dept of Mathematical Sci Thayer Hall
West Point NY 10996-1786

Nav Surface Warfare Ctr
Attn Code B07 J Pennella
17320 Dahlgren Rd Bldg 1470 Rm 1101
Dahlgren VA 22448-5100

DARPA
Attn B Kaspar
3701 N Fairfax Dr
Arlington VA 22203-1714

Hicks & Associates, Inc
Attn G Singley III
1710 Goodrich Dr Ste 1300
McLean VA 22102

Palisades Inst for Rsrch Svc Inc
Attn E Carr
1745 Jefferson Davis Hwy Ste 500
Arlington VA 22202-3402

Distribution (cont'd)

US Army Rsrch Lab
Attn AMSRL-SE-RM B Bender
Attn AMSRL-SE-RM S Stratton
Aberdeen Proving Ground MD 21005

US Army Rsrch Lab
Attn AMSRL-DD J Rocchio
Attn AMSRL-CI-LL Techl Lib (3 copies)
Attn AMSRL-CS-AS Mail & Records Mgmt
Attn AMSRL-CS-EA-TP Techl Pub (3 copies)
Attn AMSRL-SE J Mait
Attn AMSRL-SE-R A Sindoris
Attn AMSRL-SE-R B Wallace
Attn AMSRL-SE-RM C Ly
Attn AMSRL-SE-RM E Burke

US Army Rsrch Lab (cont'd)
Attn AMSRL-SE-RM G Goldman (30 copies)
Attn AMSRL-SE-RM H Dropkin (5 copies)
Attn AMSRL-SE-RM J Silverstein
Attn AMSRL-SE-RM J Silvious
Attn AMSRL-SE-RM R Wellman
Attn AMSRL-SE-RM T Pizzillo
Attn AMSRL-SE-RU B Scheiner
Attn AMSRL-SE-RU J Sichina
Attn AMSRL-SE-RU R Damarla
Attn AMSRL-SE-RU R Innocenti
Adelphi MD 20783-1197

REPORT DOCUMENTATION PAGE

Form Approved
OMB No. 0704-0188

1. AGENCY USE ONLY *(Leave blank)*

2. REPORT DATE May 1999

3. REPORT TYPE AND DATES COVERED Final, Oct 1997 to Oct 1998

4. TITLE AND SUBTITLE High-Frequency Autofocus Algorithm for Noncooperative ISAR

5. FUNDING NUMBERS
DA PR: AH16
PE: 62120A

6. AUTHOR(S) Geoffrey H. Goldman and Herbert Dropkin

7. PERFORMING ORGANIZATION NAME(S) AND ADDRESS(ES)
U.S. Army Research Laboratory
Attn: AMSRL-SE-RM email: ggoldman@arl.mil
2800 Powder Mill Road
Adelphi, MD 20783-1197

8. PERFORMING ORGANIZATION REPORT NUMBER
ARL-TR-1890

9. SPONSORING/MONITORING AGENCY NAME(S) AND ADDRESS(ES)
U.S. Army Research Laboratory
2800 Powder Mill Road
Adelphi, MD 20783-1197

10. SPONSORING/MONITORING AGENCY REPORT NUMBER

11. SUPPLEMENTARY NOTES
ARL PR: 8NE4TD
AMS code: 622120.H16

12a. DISTRIBUTION/AVAILABILITY STATEMENT Approved for public release; distribution unlimited.

12b. DISTRIBUTION CODE

13. ABSTRACT *(Maximum 200 words)*

High-quality automatic target recognition algorithms implemented using a real-beam radar require imagery with resolved target characteristics. This report presents an iterative motion parameter estimation algorithm that improves the quality of high-resolution two-dimensional inverse synthetic aperture radar (ISAR) images. The algorithm uses the derivative of the phase history of isolated point scatterers to estimate the initial conditions for the target motion parameters of a maneuvering vehicle. The algorithm was tested using simulated data. We report on the agreement between the actual and estimated values of range and entropy.

14. SUBJECT TERMS
motion compensation, image, maneuver

15. NUMBER OF PAGES
32

16. PRICE CODE

17. SECURITY CLASSIFICATION OF REPORT	**18. SECURITY CLASSIFICATION OF THIS PAGE**	**19. SECURITY CLASSIFICATION OF ABSTRACT**	**20. LIMITATION OF ABSTRACT**
Unclassified	Unclassified	Unclassified	UL

NSN 7540-01-280-5500

Standard Form 298 (Rev. 2-89)
Prescribed by ANSI Std. Z39-18
298-102